Nano Energy 38 (2017) 263–270

Contents lists available at ScienceDirect

Nano Energy

journal homepage: www.elsevier.com/locate/nanoen

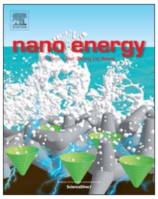

Full paper

A new metallic carbon allotrope with high stability and potential for lithium ion battery anode material

Jie Liu[a,b,c], Tianshan Zhao[a,b,c], Shunhong Zhang[a,b,c], Qian Wang[a,b,c,*]

[a] Center for Applied Physics and Technology, Peking University, Beijing 100871, China
[b] Department of Materials Science and Engineering, College of Engineering, Peking University, Beijing 100871, China
[c] Collaborative Innovation Center of IFSA (CICIFSA), Shanghai Jiao Tong University, Shanghai 200240, China

ARTICLE INFO

Keywords:
Metallic carbon
Global structure search
Structural stability
Li-ion battery
Anode material

ABSTRACT

Metallic carbon has been extensively studied for its potential novel applications in catalysis, superconductivity, and electronic devices. Currently, the design of metallic carbon is mainly by educated intuition which could miss some more stable allotropes. Here we carry out a global structure search on the potential energy surface, and identify a new three-dimensional (3D) metallic carbon phase, termed Hex-C_{18}, which is energetically more favorable than most of the previously identified 3D metallic carbon allotropes. Using state-of-the-art theoretical calculations, we show that Hex-C_{18} not only possesses a high thermodynamic stability, large heat capacity, high Debye stiffness, anisotropic elasticity, and super hardness, but also is a promising anode material for lithium ion batteries (LIBs). As compared to graphite commercially used in LIBs, Hex-C_{18} exhibits a lower Li diffusion energy barrier and a higher Li capacity because of its intrinsic metallicity and regular porosity. In addition, the simulated x-ray diffraction of Hex-C_{18} matches well with a previously unidentified low-angle diffraction peak in experimental XRD spectra of detonation soot, implying the possibility of its existence in the specimen. This study expands the family of metallic carbon, and may open a new frontier in design of high performance anode materials for LIBs as well.

1. Introduction

With versatile flexibilities of bonding in *sp*-, sp^2- and sp^3-hybridizations, carbon exhibits an amazing ability to form a tremendous number of allotropes with many unique physical and chemical properties [1,2]. Among the rich carbon phases, metallic carbon has attracted increasing interest in recent years because of its fascinating properties. It was found that metallic carbon displays a superior catalytic effect [3] attributed to its high density of states (DOS) at the Fermi level. For instance, metallic carbon nanotubes have been used as electrodes for electrocatalysis [4], and metallic carbon nanotube networks can dramatically increase the electrocatalytic activities of an enzyme-based electrode [4]. It was reported that metallic carbon can be magnetic when the Stoner-like criterion is satisfied [5]. In addition, it has been demonstrated, both theoretically and experimentally, that metallic carbon can exhibit strong phonon-plasmon coupling [6], negative differential resistance [7], and superconductivity [8,9]. Therefore, besides the *conventional* semiconducting or insulating carbon structures, metallic carbon has significantly broadened the application of carbon materials.

Since the pioneering work of Hoffmann and his colleagues [10,11], further exploration of three-dimensional (3D) metallic carbon allotropes has received considerable attention either for fundamental research or practical applications. All 3D metallic carbon structures studied thus far can be classified into three groups based on the nature of their bonding: all-sp^2 structures [10,12,13], sp^2-sp^3 hybrid structures [11,14–17], and all distorted sp^3 structures [18–20]. Recently two new 3D metallic carbon structures, H_{18} carbon [17] and Tri-C_9 carbon [20], have been predicted. The former has a hexagonal primitive cell containing 18 carbon atoms with an sp^2-sp^3 hybrid bonding network, while the latter is a trigonal system composed solely of distorted sp^3 hybridized carbon atoms. They have lower binding energy than some previously studied 3D metallic structures such as T6 carbon [17,20]. However, these two structures are constructed by physical and chemical intuition. Thus, some low-energy allotropes can be easily missed because of the complex potential energy surface. Here, based on the particle swarm optimization method combined with first principles calculations, we find a new 3D metallic carbon allotrope, Hex-C_{18}, which is thermodynamically more stable than both H_{18} carbon and Tri-C_9 carbon, and many other previously identified

---

[*] Corresponding author at: Center for Applied Physics and Technology, Peking University, Beijing 100871, China.
E-mail address: qianwang2@pku.edu.cn (Q. Wang).

http://dx.doi.org/10.1016/j.nanoen.2017.05.017
Received 7 February 2017; Received in revised form 14 April 2017; Accepted 8 May 2017

metallic carbon phases. We also demonstrate that Hex-C_{18} exhibits interesting thermodynamic, mechanical, and electronic properties, in particular, its potential as an anode material for Li-ion batteries.

2. Computational methods

We employ the efficient particle swarm optimization (CALYPSO) code [21,22] to search for low-energy 3D metallic carbon structures at ambient pressure. This efficient structure prediction method is specially designed to search for stable or metastable structures with only the knowledge of chemical composition at given external pressures. The successful applications and the details of the method are described elsewhere [23,24], The unit cell we used contains eighteen carbon atoms compatible with the size of the recently reported Tri-C_9 carbon and H_{18} carbon allotropes. Lattice parameters and atomic positions of the searched structures are further relaxed using density functional theory (DFT) within the generalized gradient approximations (GGA) [25] and the projector augmented wave (PAW) method [26], as implemented in the Vienna *Ab initio* Simulation Package (VASP) [27]. The electronic exchange-correlation interaction is incorporated using Perdew-Burke-Ernzerhof (PBE) functional [25]. The effect of van der Waals (vdW) interaction is taken into account using the semi-empirical long-range dispersion correction by Grimme (PBE-D2 method) [28]. The Heyd-Scuseria-Ernzerhof (HSE06) hybrid functional [29,30] are also used for the high accuracy of electronic structure calculations. The plane-wave cutoff energy for wave function is set to 500 eV. For structure optimization, the convergence thresholds are set to 10^{-4} eV and 10^{-3} eV/Å for total energy and force component, respectively. Monkhorst-Pack k-mesh of 7×7×21 for Hex-C_{18} is adopted to represent the first Brillouin zone. *Ab initio* molecular dynamics (AIMD) simulations at different temperatures are performed using the canonical ensemble (NVT) with the Nosé thermostat [31] to examine thermal stability. Phonon spectrum calculation is carried out using the linear response method within density functional perturbation theory [32] as implemented in the Phonopy code [33].

3. Results and discussion

3.1. Structure and stability

By CALYPSO search, the recently reported H_{18} carbon with $P6/mmm$ (D_{6h}^1) symmetry [17] is reproduced, and an energetically more stable hexagonal structure with space group $P6_3/mcm$ (D_{6h}^3) is discovered, which contains 18 atoms per unit cell, thus named Hex-C_{18}. As show in Fig. 1, there are two chemically nonequivalent carbon atoms in the primitive cell: one is the sp^3-hybridized carbon atoms at the 6 g (0.000, 0.555, 0.250) site, denoted as C1, colored in yellow, and the other is the sp^2-hybridized carbon atoms occupied the 12j (0.255, 0.429, 0.250) site, denoted as C2, colored in dark red. This structure can be considered as a 3D assembly of the sp^3 and sp^2 carbon chains, as shown in Fig. 1c. The optimized lattice constants of Hex-C_{18} are $a = b$ =8.36 Å, and c =2.46 Å. This unique configuration of Hex-C_{18} forms a porous structure with a density of 2.41 g/cm^3 (see Table 1) which is comparable to that of graphite (2.24 g/cm^3). The nanopores could accommodate other species such as atoms or molecules for further functionalization [34].

To study the effect of the van der Waals (vdW) interaction on the geometry of Hex-C_{18}, we recalculate the lattice parameters and its relative energy with respect to graphite by using the PBE functional with semiempirical vdW correction [28]. For comparison, the calculations for diamond and graphite are also carried out. The calculated results are given in Table S1 as Supplementary information, which shows that the lattice parameters and relative energies calculated with and without the semiempirical vdW correction are almost same, suggesting that the effect of vdW interaction on the geometry of Hex-C_{18} is subtle and negligible. Therefore, the following computations of the thermodynamic and mechanical properties of Hex-C_{18} are carried out using the standard PBE functional.

To further investigate the energetic stability of Hex-C_{18}, we calculate its total energy as a function of the volume. For comparison, calculations are also carried out for graphite, diamond, bct-C_4 [35], and the recently predicted metallic carbon phases, including T6 [15], H_{18} [17], K_6 [19] and Tri-C_9 [20] carbons. The results are given in Fig. 2a and Table 1, which shows that except for graphite and diamond, Hex-C_{18} has the lowest energy. In particular, it is energetically more favorable than the recently identified 3D metallic carbon allotropes (the T6, H_{18}, K_6 and Tri-C_9 carbon phases). To understand the origin of the high energetic stability of this new phase, we investigate its bonding feature. The calculated bond length of the sp^2-sp^2 bond in the sp^2-hybridized zigzag chains is 1.41 Å, which is very close to that of graphene (1.42 Å). For the sp^3-sp^3 bond in the sp^3-hybridized chains, the calculated bond length is 1.54 Å, very close to that of diamond (1.53 Å). The average bond angle of the sp^2-hybridized carbon atoms is 120.5°, while average bond angle of the sp^3-hybridized carbon atoms is 110.5°. These are respectively quite close to the ideal bonding angles of 120° and 109.5° in graphene and diamond, thus leading to the high energetic stability of Hex-C_{18}.

To examine the stability of Hex-C_{18}, we first calculate its phonon band structure. As shown in Fig. 2b, the absence of imaginary modes in the whole Brillouin zone confirms that Hex-C_{18} is dynamically stable. We then perform AIMD simulation at 300 K to verify the thermal stability of Hex-C_{18} at room temperature. We use a 2×2×4 large supercell to minimize the constraint of periodic boundary condition. The simulated results are plotted in Fig. 3, which clearly shows that the skeleton of this structure remains almost intact after heating for 8 ps (*ps*) with a time step of 1 femtosecond (*fs*), and the average value of the total potential energy remains almost constant during the whole simulation, confirming that Hex-C_{18} is thermally stable at room temperature. We further increase the heat bath temperature to 600 K, and then to 1200 K, respectively. As shown in the snapshots of Fig. 3, the atomic configuration at the end of the MD simulation at 1200 K has no obvious distortions, and the potential energy fluctuates around its average value. Hence, the structure is confirmed to be thermally stable even at high temperatures (1200 K). We recall that the two previously proposed 3D metallic carbon structures, T6 [15] carbon and K_6 [19] carbon, become unstable when heated to above 500 K [17], suggesting that Hex-C_{18} can withstand much higher temperatures compared to the other metallic carbon structures. The favorable thermal stability of Hex-C_{18} implies that this new carbon allotrope is separated by high energy barriers from other local minima on the potential energy surface (PES).

To verify the mechanical stability, we calculate the elastic constants of Hex-C_{18}. The calculated results are listed in Table 2. In general, for a hexagonal lattice, only C_{11}, C_{33}, C_{44}, C_{12}, and C_{13} are independent. Also, the linear elastic constants of a mechanically stable 3D hexagonal lattice have to obey the Born-Huang criteria: $C_{44} > 0$, $C_{11} > C_{12}$, $(C_{11} + 2C_{12})C_{33} > 2C_{13}^2$ [36]. We find that the calculated constants of Hex-C_{18} satisfy all of the criteria, hence the Hex-C_{18} is mechanically stable.

3.2. Thermodynamic properties

Based on the calculated phonon spectrum, a series of thermodynamic properties can be derived. Here we concentrate on the constant volume lattice heat capacity (denoted as lattice capacity for convenience of discussion without ambiguity) and Debye temperature of Hex-C_{18}. The calculated phonon heat capacity with respect to temperature is plotted in Fig. 4a. The heat capacity can also be expressed as a function of phonon DOS [37]. The Debye temperature $\Theta_D = h\nu_D/k_B$ is determined by fitting the calculated C_V-T curve using Debye model. The fitted Debye temperature Θ_D (T) is given in Fig. 4b, which shows that the Θ_D (T) is as high as 1600 K at room temperature. Since the vibrational frequency is proportional to the square root of the stiffness

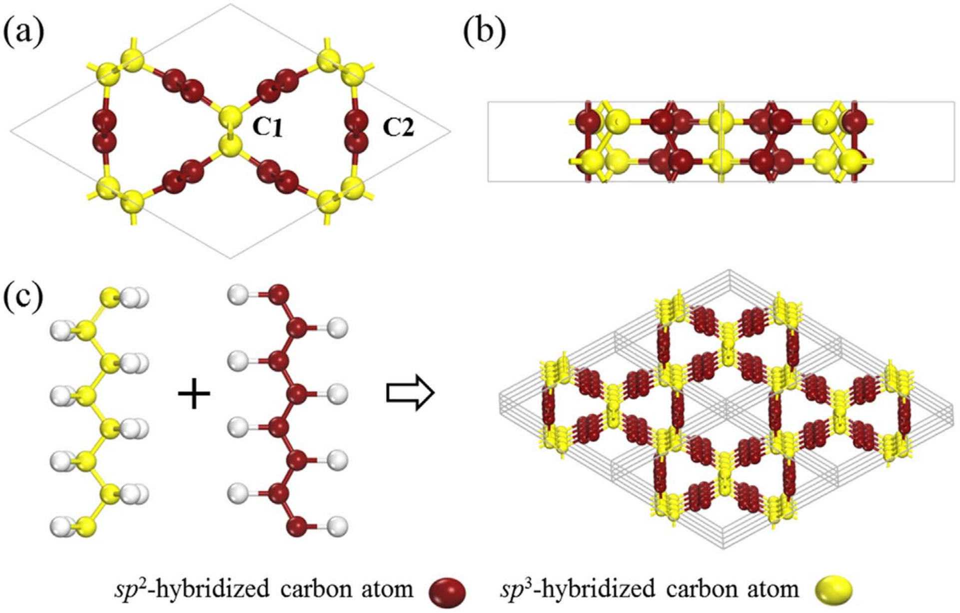

Fig. 1. (a) Top view and (b) side view of the optimized structure of Hex-C_{18}. (c) A schematic illustration of a possible synthesis strategy for Hex-C_{18} by using C-H chains via dehydrogenation and assembly.

Table 1
Crystal system, space group, calculated equilibrium density ρ (in g/cm^3), and cohesive energy E_{coh} (in eV/atom) of Hex-C_{18} and some other carbon allotropes including diamond, graphite, bct-C_4, T6, H_{18}, K_6, and Tri-C_9 carbon phases.

	System	Groups	ρ	E_{coh}
Hex-C_{18}	Hex	$P6_3/mcm$	2.41	7.70
Diamond	Cub	$Fd\bar{3}m$	3.55	7.83
Graphite	Hex	$P6_3/mmc$	2.24	7.96
bct C_4	Tetra	$I4/mmm$	3.42	7.63
T6	Tetra	$P4_2/mmc$	3.06	7.37
H_{18}	Hex	$P6/mmm$	3.14	7.49
K_6	Cub	$I4_132$	2.10	6.48
Tri-C_9	Hex	$R32$	3.23	6.86

within the harmonic approximation, Θ_D can be used as a measurement of the "stiffness" of solids [37]. Therefore, from Fig. 4b we see that Hex-C_{18} displays a large Debye stiffness because of its high Debye temperature.

As phonons are subjected to the Bose-Einstein distribution, the weighted phonon DOS (g(ν)W($h\nu/k_BT$)) describes the contribution of

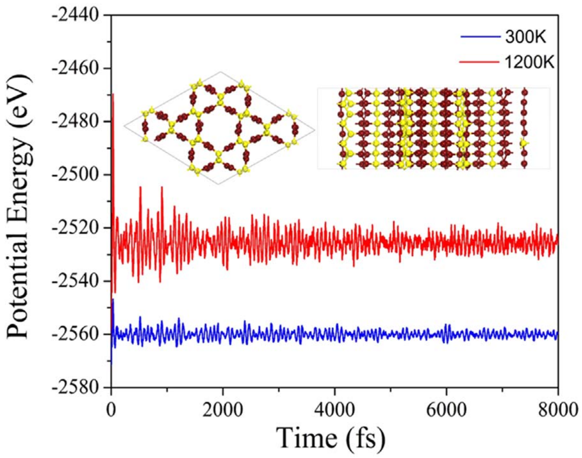

Fig. 3. Total potential energy fluctuation during AIMD simulation at 300 K and 1200 K. The inset shows the atomic configurations (2×2×4 supercell) at the end of AIMD simulations at 1200 K.

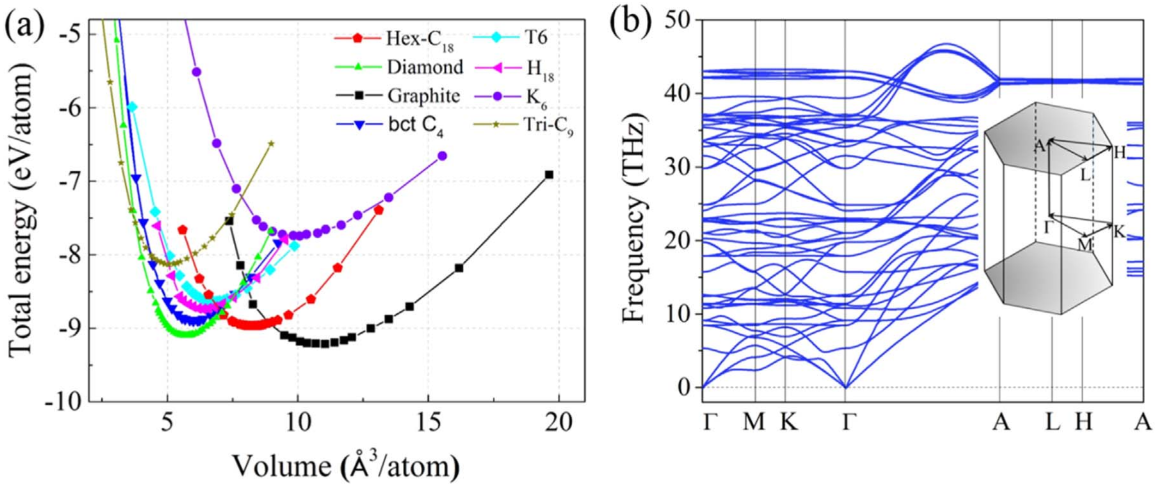

Fig. 2. (a) Volume dependence of total energy per atom for Hex-C_{18}, diamond, graphite, bct C_4, T6, H_{18}, K_6, and Tri-C_9 carbons. (b) Phonon band structure of Hex-C_{18}. The inset shows the first Brillouin zone and the high symmetry k point path.

Table 2
Calculated elastic constants (C_{ij} in GPa), Young's moduli ($Y_{x/y/z}$ in GPa), bulk moduli (B in GPa), shear modulus (G in GPa) and hardness (H_v in GPa) of diamond and Hex-C_{18}.

	Diamond	Hex-C_{18}
C_{11}	1024.1 (1085.5[a])	523.5
C_{33}	–	1132.8
C_{44}	563.1 (582.1[a])	244.1
C_{12}	119.3 (113.4[a])	124.2
C_{13}	–	56.7
Y_x	999.2 (1064.0[a])	492.4
Y_y	–	492.4
Y_z	–	1122.9
B	420.9 (437.4[a])	282.9
G	518.7 (541.6[a])	254.6
H_v	93.4[b]/92.1[c]	42.2[b]/80.8[c]

[a] Ref. [16].
[b] Chen's model.
[c] Gao's model.

vibrational modes with a certain frequency to the heat capacity. The frequency and temperature dependence of the weighted phonon DOS is plotted in Fig. 4c. We find that the distribution of weighted phonon DOS tends to concentrate around the low-frequency region with decreasing temperature, indicating that the heat capacity at low temperature is mainly contributed by the low-frequency states. As shown in Fig. 4d, at low temperature around 50 K the weighted phonon DOS only distributes in the low-frequency region around 200 cm^{-1}, confirming that the heat capacity at low temperature is contributed by low-frequency phonons. Since the heat capacity defined by the *Debye model* is proportional to the cross section of *Frequency-Phonon DOS* at a given temperature, a larger amount of heat is required to increase the temperature by one Kelvin when the cross section is larger. Because Hex-C_{18} has more vibrational states than graphite [37] over the entire frequency region, Hex-C_{18} exhibits larger heat capacity. For comparison, the weighted phonon DOS of T6, H_{18}, and Tri-C_9 is also calculated, respectively, following the above procedure.. The 3D plots of the weighted phonon DOS as a function of frequency and temperature, and the cross sections of the weighted phonon DOS at 50, 150, 300, 600, and 900 K for the T6, H_{18}, and Tri-C_9 carbon phases are respectively plotted in Fig. S2. We find that Hex-C_{18} possesses a larger heat capacity than T6, H_{18}, and Tri-C_9 in low temperature region (T < 150 K), because its cross sections of Frequency-Phonon DOS are larger than those of the three metallic carbon allotropes in this temperature region. This is attributed to the larger phonon DOS of Hex-C_{18} as compared to that of T6, H_{18}, and Tri-C_9 in the low-frequency region, which makes decisive contribution to the heat capacity at low temperature.

3.3. Mechanical properties

Because of its unique configuration, the mechanical properties of Hex-C_{18} are highly anisotropic. Along the extended direction of the sp^2-hybridized zigzag chains (z-direction), Hex-C_{18} exhibits ultra-high stiffness with elastic constant (C_{33}) and the Young's modulus of Hex-C_{18} even larger than the corresponding values of diamond, while in the radial direction (x- and y-direction), the elastic constants of Hex-C_{18} (C_{11} and C_{22}) are about half the value of diamond. The bulk modulus (B) and shear modulus (G) of Hex-C_{18} are also calculated with the Voigt-Reuss-Hill approximation [38] (see Table 2).

We also evaluate the Vickers hardness (H_v) of Hex-C_{18} using two different empirical models developed by Chen et al. [39]. and Gao et al. [40], respectively. In Chen's model, the hardness of polycrystalline materials is correlated with the product of the squared Pugh's modulus ratio and the shear modulus ($H_v=2(k^2G)^{0.585} - 3$ where $k= G/B$ is Pugh's modulus ratio) [39]. The H_v value of Hex-C_{18} calculated using Chen's model is 42.2 GPa. Gao's model, however, correlates Vickers hardness with the electron density of valence electrons per Å^3, the ionicity of the chemical bond in the crystal on the Philips scale, and the bond length [40]. Based on the formula for Gao's model, the H_v value of Hex-C_{18} is calculated to be 80.8 GPa, which is comparable to that of diamond evaluated using the same model (see Table 2). Recently, the

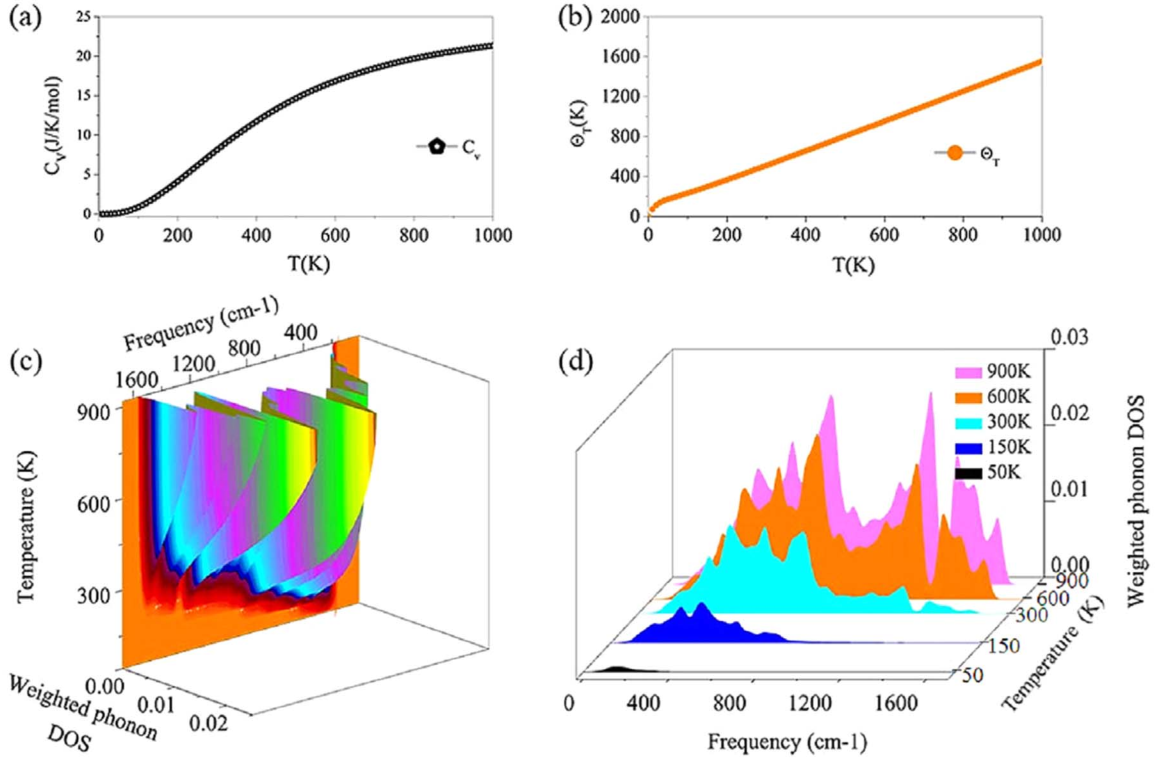

Fig. 4. (a) Heat capacity, and (b) Debye temperature of the Hex-C_{18} with respect to temperature; (c) 3D plot of the weighted phonon DOS as a function of frequency and temperature; (d) cross sections of the weighted phonon DOS at 50, 150, 300, 600, and 900 K.

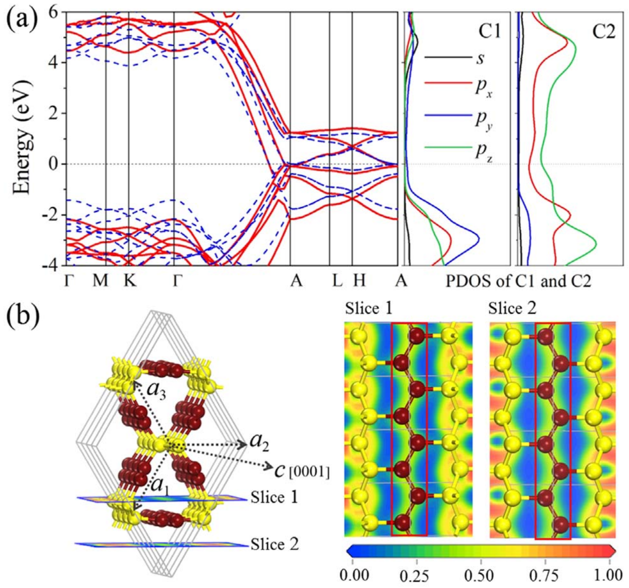

Fig. 5. (a) Electronic band structures calculated using the DFT-GGA/PBE (blue dashed lines) and the HSE06 hybrid functional (red solid lines), and projected DOS for C1 and C2 atom at DFT-GGA/PBE level of Hex-C_{18}. (b) Two ELF slices parallel to the $(10\bar{1}0)$ crystal surface of Hex-C_{18}.

hardness value of anisotropic compounds evaluated using Gao's model was found to be overestimated [41,42]. Therefore the hardness of Hex-C_{18} is deduced to be approximately between 42.2 GPa to 80.8 GPa. According to the generally accepted definition that superhard materials are those with the H_v value exceeding 40 GPa [43], Hex-C_{18} is a superhard material.

3.4. Electronic properties

The electronic properties of Hex-C_{18} are studied by calculating its electronic band structure. As shown in Fig. 5a, for the band structure calculated by using the DFT-GGA/PBE functional, the Fermi level crosses the highest occupied band in the high symmetry K point path of Γ(0, 0, 0)→A(0, 0, 0.5), indicating that Hex-C_{18} is metallic. To further confirm the metallicty of Hex-C_{18}, the band structure is recalculated using the HSE06 functional, which is known to provide more accurate band structures as the electron Coulomb screening is more accurately treated in the exchange-correlation energy of electrons in solids [29,30]. The result is also presented in Fig. 5a. One can see that there is a systematic up/down shift for the conduction/valence band, as compared to the PBE band structure. However, the metallic fracture remains unchanged at the HSE06 level, suggesting the metallicty of Hex-C_{18} is an intrinsic property. The effect of the vdW interaction on the band structure is further checked, and found to be neglected as the band structure remains almost unchanged when the vdW interaction is included (see Fig. 2S for details). Most of the strong covalent carbon allotropes with superhardness are insulators or semiconductors, such as diamond, lonsdaleite [44], M-carbon [45] and Z-carbon [46]. Compared with these carbon allotropes, Hex-C_{18} is a superhard material with conductivity, making it a promising candidate for applications in petroleum drilling tools, cutting tools, and special wear-resistant parts [16].

To understand the origin of the metallicity, we calculate the DOS projected onto the two nonequivalent carbon atoms, C1 and C2 as shown in Fig. 5a, which clearly indicates that the dominant contribution to the DOS around the Fermi level comes from the $2p_z$ orbitals of C2, the contribution from the C2 $2p_y$ orbitals is small, and that from C1 is negligible. The highly dispersive bands (with band width larger than 4 eV) around the Fermi level along the Γ-A path imply possible existence of delocalized valance electrons in this compound. We further calculate the electron localization function (ELF) of Hex-C_{18} to identify its character of electron delocalization. ELF, first introduced by Becke and Edgecombe as a "simple measure of electron localization in atomic and molecular systems [47]," has been widely used in describing electron delocalization in molecules and solids [48–50]. ELF is a uniquely defined dimensionless quantity, and only takes values in the range between 0 and 1, where 1 refers to the fully localized electrons, and 0.5 corresponds to fully delocalized electrons, while 0 represents very low charge density [47]. As shown in Fig. 5b, by calculating the ELF slices parallel to the $(10\bar{1}0)$ crystal surface of Hex-C_{18}, 1D extended channels with ELF values of 0.5 (highlighted by the red rectangle) are found along the extended direction of the sp^2-hybridized zigzag chains ([0001]). Since the value ELF=0.5 in inhomogeneous systems indicates regions where the electrons are fully delocalized, the 1D extended channels can be confirmed as conducting channels. Thus, we conclude that there are 1D conducting channels along the [0001] direction in the structure of Hex-C_{18} formed by delocalized electrons of the sp^2-hybridized carbon atoms.

The extended direction of the 1D metallic channels in the real space ([0001] direction) corresponds to the direction from the Γ point to the A point in the reciprocal space. Thus, the velocity of carriers moving in the 1D conducting channels can be calculated from the formula $\vec{\upsilon}_{\vec{k}} = \hbar \frac{d\mathcal{E}_{\vec{k}}}{d\vec{k}}$ ($\mathcal{E}_{\vec{k}}$ is the energy and $\vec{k}$ is the wavevector).

Based on the band structure obtained at the PBE level, the highest carrier velocity from the Γ point to the A point is calculated to be 1.25×10^6 m s^{-1}, which is even larger than that of graphene (0.86×10^6 m s^{-1}) calculated using the same formula. Our results for graphene is in good agreement with the value of 0.86×10^6 m s^{-1} obtained by Bu et al. [16], confirming the validity of our calculations. In comparison, around the Fermi level, the electronic bands along the A-H and L-H direction in the Brillouin zone are nearly flat. Hence, in the plane normal to the 1D conducting channels, carriers move rather slowly. So Hex-C_{18} with 1D conducting channels exhibits highly anisotropic transport properties. The highly anisotropic transport properties of Hex-C_{18} with 1D conducting channels may have potential applications in microelectronic devices [51].

3.5. Application as an anode material for LIBs

Besides the above mentioned possible applications of metallic carbon in catalysis, magnetism, superconducting and microelectronic devices, another promising field is as an anode material for LIBs, since the regular porousity and intrinsic metallicity of metallic carbon provide the basis for storing and transporting Li ions with good conductivity. However, this has not yet been explored. Here we study Hex-C_{18} as a model. We systematically explore the potential of Hex-C_{18} as a Li-ion battery anode material by studying the Li binding and diffusion behavior as well as the theoretical capacity.

We first investigate the binding of a single Li atom into the 3D Hex-C_{18} phase. To avoid the interaction between the Li atoms, we adopt a 1×1×6 supercell. The effect of the vdW interaction on the geometry of the Li adsorbed Hex-C_{18}, and the thermodynamics and kinetic of Li atoms in the structure of Hex-C_{18} is taken into account by using semiempirical long-range dispersion correction (the PBE-D2 functional) [28]. Three possible initial adsorption sites for Li atom are examined with high geometric symmetry, marked as Li_I, Li_{II}, and Li_{III} in Fig. 6a, where Li_I is for the triangle hollow site, Li_{II} is for the hexagonal hollow site, and Li_{III} is for the edge site of the "groove" formed by an 8-membered carbon rings. To check the binding strength of Li on these sites, we calculate the Li binding energy (E_b), defined as $E_b = (E_{Li_x\text{-Hex-}C_{18}} - E_{Hex\text{-}C_{18}} - x\mu_{Li})/x$, where $E_{Li_x\text{-Hex-}C_{18}}$/ $E_{Hex\text{-}C_{18}}$ is the total energy of the system per formula unit with /without Li, and μ_{Li} is the energy of one Li atom in Li bulk phase [52]. As shown in Fig. 6b, the calculated binding energies for the configurations with Li atom on Li_I,

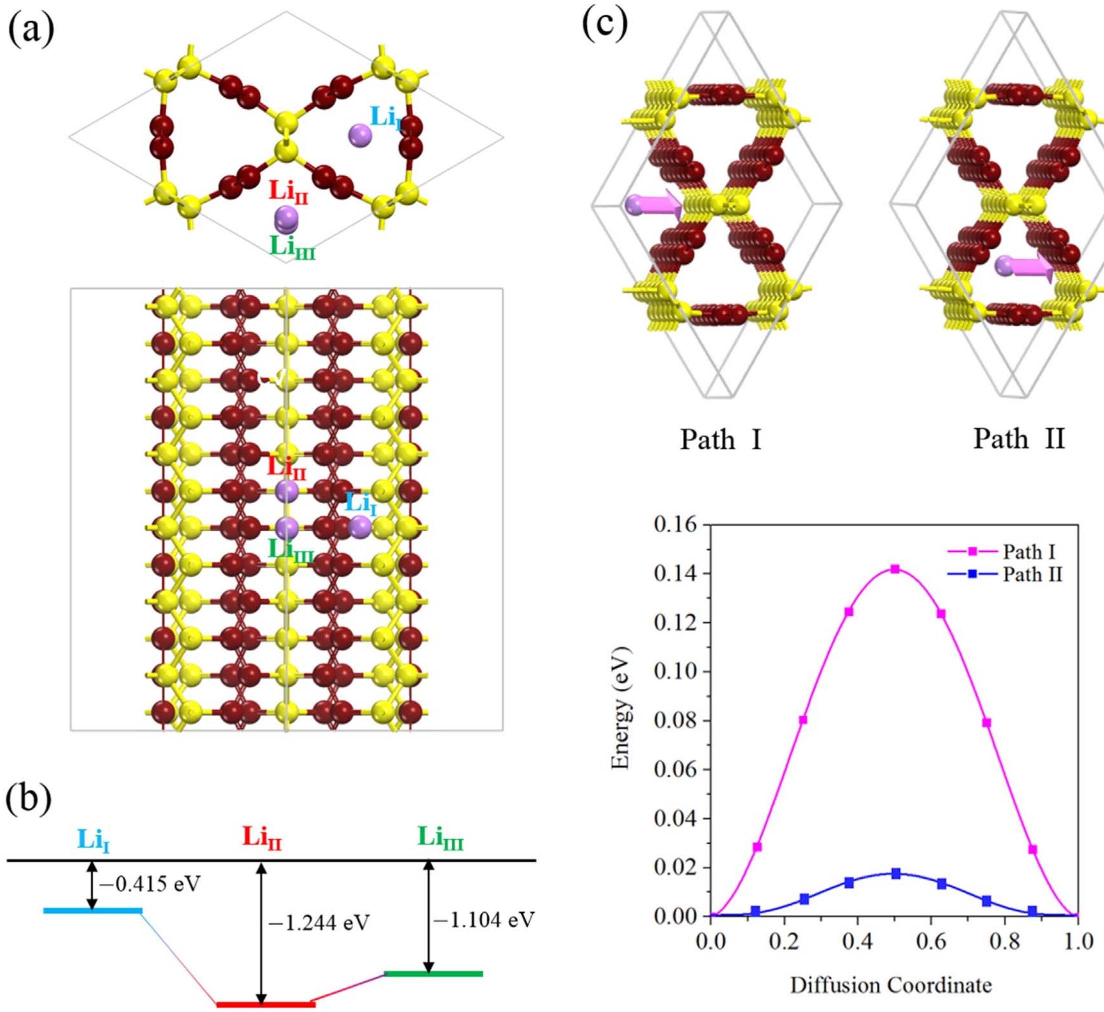

Fig. 6. (a) Top and side views of the possible Li absorption sites. (b) Binding energies of the three configurations in (a). (c) Considered migration paths of Li diffusion and the corresponding diffusion energy barrier profiles.

Li$_{II}$, and Li$_{III}$ are −0.415, −1.244, and −1.104 eV, respectively, namely, the adsorption configuration with Li on Li$_{II}$ is more stable lying 0.829 and 0.140 eV lower in energy than that of Li$_I$ and Li$_{III}$, respectively, implying that Li atom prefers the hexagonal hollow site, where each Li atom transfers 0.89 electrons to the neighboring C atoms according to the Bader charge analysis [53]. While for the configurations with Li on Li$_I$ and Li$_{III}$, the transferred charges are found to be 0.79 and 0.90 electrons, respectively, suggesting that the Li atoms in the three adsorption configurations donate most of their valance electrons and become Li ions, leading to a strong Coulomb repulsion interaction between the adsorbed Li ions thus preventing them from clustering.

We next calculate the energy barrier for Li ion diffusion. Considering the symmetry of Hex-C_{18}, we select two representative diffusive pathways: path I is along the [0001] in the hexagonal hollow channel, while path II is along the triangle hollow channel, as shown in Fig. 6c. Based on nudged elastic band (NEB) calculations, the corresponding energy barriers are found to be 0.142 and 0.018 eV, respectively, both of them are much lower than that in graphite (0.218–0.400) eV [54–56], indicating a high-rate capability of Hex-C_{18} for LIBs.

We then determine the maximum Li capacity. The top and side views of the fully Li-intercalated configuration of Hex-C_{18} are displayed in Fig. S3 in Supplementary information. The corresponding average binding energy E_b is calculated to be −0.417 eV, the binding is stronger than that of $Ti_3C_2(OH)_2$ monolayer ($Ti_3C_2(OH)_2Li_{0.5}$: 0.14 eV) [57], and is comparable to that of $Ti_3C_2(F)_2$ monolayer ($Ti_3C_2F_2Li$: 0.56 eV) [57] calculated at the same level. The theoretical specific capacity of Hex-C_{18} is 496 mAh/g, which is 1.3 times as large as that of graphite.

To further confirm the maximum Li concentration of Hex-C_{18}, we examine 100 configurations at different intermediate Li concentrations (0.250, 0.375, 0.500, 0.625, and 0.750). As shown in Fig. S4, the binding energies of these structures are all negative, indicating that Li ions can be adsorbed stably without clustering. Based on the calculated results, five stable configurations at the intermediate concentrations are found (see Fig. S5 for details). The absolute values of their binding energies are all larger than that of the fully Li-intercalated configuration and decrease gradually with increasing the Li concentration, because of the enhanced repulsive interaction between the Li ions and the reduced interaction between the Hex-C_{18} host structure and the Li ions. The existence of the stable intermediate configurations confirms the maximum Li concentration of Hex-C_{18} ($LiC_{4.5}$).

These results suggest that compared to the currently used anode material in LIB, the new metallic carbon allotrope exhibits additional benefits. More importantly, the favorable transport direction for charge carriers and Li ions in real space coincidently are exactly the same, enabling high-flux directional (electrical and ion) transport when this material is implemented as an electrode in LIB. These findings should encourage more research effort on porous metallic carbon in the future.

3.6. Possible existence of Hex-C_{18} in detonation soot

To establish the experimental connection with Hex-C_{18}, the x-ray

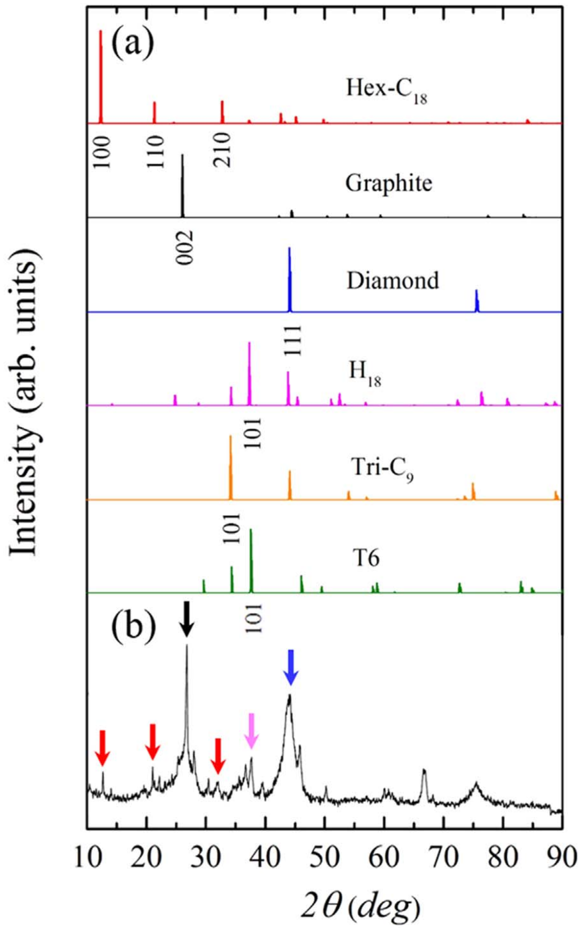

Fig. 7. Simulated XRD patterns for (a) Hex-C_{18}, graphite, diamond, H_{18}, Tri-C_9, and T6 carbons. (b) Experimental XRD pattern for the detonation soot of TNT (sample Alaska B [58]). Red, pink, black, and blue arrows indicate the peaks that match the simulated characteristic peaks of Hex-C_{18}, H_{18}, graphite, and diamond, respectively. The X-ray wavelength we adopted for simulation is 1.54059 Å.

diffraction (XRD) spectra of Hex-C_{18} are simulated and compared with the experimental data from detonation soot (sample Alaska B [58]), along with those of graphite, diamond, H_{18}, Tri-C_9 and T6 carbons in Fig. 7. In the experimental XRD spectra, clear evidence of several crystalline carbon allotropes together with a good deal of amorphous carbon can be found. As shown in Fig. 7, the two strongest experimental XRD peaks around 26.5° and 43.9° are associated with the graphite (002) and diamond (111) diffractions, respectively. The (101) peak of T6 carbon and H_{18} carbon match with the experimental XRD peak located at 37.4°. As reported by Zhao et al., the experimental XRD peak near 37.4° would be predominantly associated with H_{18} carbon rather than T6 carbon since H_{18} carbon is thermodynamically more stable than T6 carbon [17]. However, the low-angle peak of the experimental XRD spectra at 13.4° which was also observed in other detonation soot [58] does not match any previously known carbon phase. The existence of this distinct low-angle peak in different detonation XRD spectra suggest that a new crystalline carbon phase may have been produced. Our simulated XRD results show that the main (100) peak of Hex-C_{18} matches well with this previously unexplained peak at 13.4°. Meanwhile, the (110) and (210) peaks of Hex-C_{18} match the experimental XRD peaks located at 21.3° and 31.9°, respectively, indicating the presence of Hex-C_{18} in the recovered specimen produced by detonation experiments [58,59].

4. Conclusions

In summary, using particle swarm optimization techniques, we predicted a new 3D metallic carbon allotrope, Hex-C_{18}, composed of sp^2- and sp^3-hybridized carbon atoms. By performing state-of-the-art theoretical calculations, we demonstrated that the Hex-C_{18} phase is not only dynamically, thermally and mechanically stable, but also energetically more favorable than most of the previously identified 3D metallic carbon allotropes. Because of its unique atomic configuration, Hex-C_{18} exhibits exceptional properties including a large phonon heat capacity, high Debye stiffness, anisotropic elasticity, and superhardness. More importantly, for the first time, we have studied the potential applications of metallic carbon in LIBs. We found that Hex-C_{18} is a promising anode material for LIBs with a low Li diffusion energy barrier and high Li capacity. It is worth noting that battery science and technology are of current interest. The specific capacity of the commercially used graphite anode for LIB is limited to 372 mAh/g. Extensive efforts have been devoted to improving the performance but not much progress has been made during the past 25 years. Our study provides new insight into finding new materials for high performance LIBs.

Acknowledgments

This work is partially supported by grants from the National Natural Science Foundation of China (NSFC-51471004), and the National Key Research and Development Program of China (2016YFE0127300). The calculations were carried out at the High Performance Computing Platform of CAPT at Peking University, China,

Appendix A. Supplementary information

Supplementary information associated with this article can be found in the online version at doi:10.1016/j.nanoen.2017.05.017.

References

[1] V. Georgakilas, J.A. Perman, J. Tucek, R. Zboril, Chem. Rev. 115 (2015) 4744–4822.
[2] Y. Lin, Z. Zhao, T.A. Strobel, R. Cohen, Phys. Rev. B 94 (2016) 245422.
[3] C. Bergeret, J. Cousseau, V. Fernandez, J.-Y. Mevellec, S. Lefrant, J. Phys. Chem. C 112 (2008) 16411–16416.
[4] C.E. Banks, T.J. Davies, G.G. Wildgoose, R.G. Compton, Chem. Commun. (2005) 829–841.
[5] H. Ohldag, T. Tyliszczak, R. Höhne, D. Spemann, P. Esquinazi, M. Ungureanu, T. Butz, Phys. Rev. Lett. 98 (2007) 187204.
[6] S. Piscanec, M. Lazzeri, J. Robertson, A.C. Ferrari, F. Mauri, Phys. Rev. B 75 (2007) 035427.
[7] Y. Ni, K.-L. Yao, H.-H. Fu, G.-Y. Gao, S.-C. Zhu, B. Luo, S.-L. Wang, R.-X. Li, Nanoscale 5 (2013) 4468–4475.
[8] H. Terrones, M. Terrones, E. Hernández, N. Grobert, J.-C. Charlier, P. Ajayan, Phys. Rev. Lett. 84 (2000) 1716.
[9] M. Kociak, A.Y. Kasumov, S. Guéron, B. Reulet, I. Khodos, Y.B. Gorbatov, V. Volkov, L. Vaccarini, H. Bouchiat, Phys. Rev. Lett. 86 (2001) 2416.
[10] R. Hoffmann, T. Hughbanks, M. Kertesz, P.H. Bird, J. Am. Chem. Soc. 105 (1983) 4831–4832.
[11] M.J. Bucknum, R. Hoffmann, J. Am. Chem. Soc. 116 (1994) 11456–11464.
[12] G.M. Rignanese, J.C. Charlier, Phys. Rev. B 78 (2008) 125415.
[13] M. Itoh, M. Kotani, H. Naito, T. Sunada, Y. Kawazoe, T. Adschiri, Phys. Rev. Lett. 102 (2009) 055703.
[14] F.J. Ribeiro, P. Tangney, S.G. Louie, M.L. Cohen, Phys. Rev. B 74 (2006) 172101.
[15] S. Zhang, Q. Wang, X. Chen, P. Jena, Proc. Natl. Acad. Sci. 110 (2013) 18809–18813.
[16] H. Bu, M. Zhao, W. Dong, S. Lu, X. Wang, J. Mater. Chem. C 2 (2014) 2751–2757.
[17] C.-X. Zhao, C.-Y. Niu, Z.-J. Qin, X.Y. Ren, J.-T. Wang, J.-H. Cho, Y. Jia, Sci. Rep. 6 (2016) 21879.
[18] K. Iyakutti, M. Rajarajeswari, Y. Kawazoe, Phys. B 405 (2010) 3324–3327.
[19] C.-Y. Niu, X.-Q. Wang, J.-T. Wang, J. Chem. Phys. 140 (2014) 054514.
[20] Y. Cheng, R. Melnik, Y. Kawazoe, B. Wen, Cryst. Growth Des. 16 (2016) 1360–1365.
[21] Y. Wang, J. Lv, L. Zhu, Y. Ma, Phys. Rev. B 82 (2010) 094116.
[22] Y. Wang, J. Lv, L. Zhu, Y. Ma, Comput. Phys. Commun. 183 (2012) 2063–2070.
[23] Y. Wang, H. Liu, J. Lv, L. Zhu, H. Wang, Y. Ma, Nat. Commun. 2 (2011) 563.
[24] L. Zhu, H. Liu, C.J. Pickard, G. Zou, Y. Ma, Nat. Chem. 6 (2014) 644–648.

[25] J. Perdew, Phys. Rev. Lett. 78 (1997) 6.
[26] P.E. Blöchl, Phys. Rev. B 50 (1994) 17953.
[27] G. Kresse, J. Furthmüller, Phys. Rev. B 54 (1996) 11169–11186.
[28] S. Grimme, J. Comput. Chem. 27 (2006) 1787–1799.
[29] J. Heyd, G.E. Scuseria, M. Ernzerhof, J. Chem. Phys. 118 (2003) 8207–8215.
[30] J. Heyd, G.E. Scuseria, M. Ernzerhof, J. Chem. Phys. 124 (2006) 219906.
[31] S. Nosé, J. Chem. Phys. 81 (1984) 511–519.
[32] X. Gonze, Phys. Rev. B 55 (1997) 10337–10354.
[33] A. Togo, F. Oba, I. Tanaka, Phys. Rev. B 78 (2008) 134106.
[34] Z. Zhao, B. Xu, L.-M. Wang, X.-F. Zhou, J. He, Z. Liu, H.-T. Wang, Y. Tian, ACS Nano 5 (2011) 7226–7234.
[35] K. Umemoto, R.M. Wentzcovitch, S. Saito, T. Miyake, Phys. Rev. Lett. 104 (2010) 125504.
[36] F. Mouhat, F.-X. Coudert, Phys. Rev. B 90 (2014) 224104.
[37] T. Tohei, A. Kuwabara, F. Oba, I. Tanaka, Phys. Rev. B 73 (2006) 064304.
[38] R. Hill, Proc. Phys. Soc. A 65 (1952) 349.
[39] X.-Q. Chen, H. Niu, D. Li, Y. Li, Intermetallics 19 (2011) 1275–1281.
[40] F. Gao, J. He, E. Wu, S. Liu, D. Yu, D. Li, S. Zhang, Y. Tian, Phys. Rev. Lett. 91 (2003) 015502.
[41] Y.-W. Son, M.L. Cohen, S.G. Louie, Phys. Rev. Lett. 97 (2006) 216803.
[42] H. Bu, M. Zhao, Y. Xi, X. Wang, H. Peng, C. Wang, X. Liu, EPL (Europhys. Lett.) 100 (2012) 56003.
[43] J. Qin, D. He, J. Wang, L. Fang, L. Lei, Y. Li, J. Hu, Z. Kou, Y. Bi, Adv. Mater. 20 (2008) 4780–4783.
[44] Q.-K. Li, Y. Sun, Z.-Y. Li, Y. Zhou, Scr. Mater. 65 (2011) 229–232.
[45] Q. Li, Y. Ma, A.R. Oganov, H. Wang, H. Wang, Y. Xu, T. Cui, H.-K. Mao, G. Zou, Phys. Rev. Lett. 102 (2009) 175506.
[46] M. Amsler, J.A. Flores-Livas, L. Lehtovaara, F. Balima, S.A. Ghasemi, D. Machon, S. Pailhes, A. Willand, D. Caliste, S. Botti, Phys. Rev. Lett. 108 (2012) 065501.
[47] A.D. Becke, K.E. Edgecombe, J. Chem. Phys. 92 (1990) 5397–5403.
[48] A. Savin, A. Becke, J. Flad, R. Nesper, H. Preuss, H.G. von Schnering, Angew. Chem. Int. Ed. Engl. 30 (1991) 409–412.
[49] A. Savin, O. Jepsen, J. Flad, O.K. Andersen, H. Preuss, H.G. von Schnering, Angew. Chem. Int. Ed. Engl. 31 (1992) 187–188.
[50] B. Silvi, A. Savin, Nature 371 (1994) 683–686.
[51] J. Lahiri, Y. Lin, P. Bozkurt, I.I. Oleynik, M. Batzill, Nat. Nanotechnol. 5 (2010) 326–329.
[52] E. Lee, K.A. Persson, Nano Lett. 12 (2012) 4624–4628.
[53] W. Tang, E. Sanville, G. Henkelman, J. Phys. Condens. Matter 21 (2009) 084204.
[54] K. Persson, V.A. Sethuraman, L.J. Hardwick, Y. Hinuma, Y.S. Meng, A. van der Ven, V. Srinivasan, R. Kostecki, G. Ceder, J. Phys. Chem. Lett. 1 (2010) 1176–1180.
[55] C. Uthaisar, V. Barone, Nano Lett. 10 (2010) 2838–2842.
[56] J. Liu, S. Wang, Q. Sun, Proc. Natl. Acad. Sci. 114 (2017) 201618051.
[57] Q. Tang, Z. Zhou, P. Shen, J. Am. Chem. Soc. 134 (2012) 16909–16916.
[58] D. Pantea, S. Brochu, S. Thiboutot, G. Ampleman, G. Scholz, Chemosphere 65 (2006) 821–831.
[59] P. Chen, F. Huang, S. Yun, Carbon 41 (2003) 2093–2099.

Jie Liu received his BSc degree in 2014 from Huazhong University of Science and Technology, China. He is currently a PhD student majored in mechanics and advanced materials in the Center for Applied Physics and Technology of Peking University supervised by professor Qian Wang. His current research interests include the design and simulation of new metallic materials based on non-metal light elements and design of novel 2D materials for energy and environment applications.

Tianshan Zhao received his BSc degree majored in physics in 2012 from Nanjing University, China. He is currently a PhD student majored in mechanics and advanced materials in the Center for Applied Physics and Technology of Peking University supervised by professor Qian Wang. His current research interest is computational study of lithium ion batteries, CO_2 capture and conversion. He is now a student in the CSC cooperative project program at the Virginia Commonwealth University.

Shunhong Zhang received his Ph.D. degree (Major: mechanics and advanced materials; supervisor: Professor Qian Wang) in July 2016 from Peking University. His current research interests include computational design and study of novel carbon based materials and low dimensional materials, topological quantum materials and high temperature superconductors. He is now a postdoc fellow in Institute for Advanced Study, Tsinghua University, and a visiting scholar in the University of Utah.

Qian Wang received her PhD in Materials Science from Tohoku University (Japan) in 2011. She is a professor at Peking University, China. Her current research interests include high energy density physics, magnetism of diluted magnetic semiconductors and carbon-based materials, and computational design of new materials. Dr. Wang was selected among the “Most Cited Chinese Researchers” in Physics & Astronomy in 2014, 2015 and 2016, and received “MID-CAREER AWARD” for outstanding scientific contribution in the area of Computational Material Science, issued by Asian Consortium on Computational Materials Science in 2016.